Post-Print

This is the accepted version of:

The final publication is available at https://doi.org/10.1016/j.actaastro.2019.10.043

Access to the published version may require subscription.

When citing this work, cite the original published paper.

Permanent link to this version
http://hdl.handle.net/11311/1121799

Initial Orbit Determination with the Multibeam Radar Sensor BIRALES

Matteo Losacco[a,*], Pierluigi Di Lizia[a], Mauro Massari[a], Giovanni Naldi[b],
Giuseppe Pupillo[b], Germano Bianchi[b], Jan Siminski[c]

[a]*Department of Aerospace Science and Technology, Politecnico di Milano, Via G. La Masa 34, 20156 Milano, Italy*
[b]*Italian National Institute for Astrophysics – Institute for Radio Astronomy, Via P. Gobetti 101, 40129 Bologna, Italy*
[c]*European Space Operations Centre (ESOC/ESA), Robert-Bosch-Straße 5, 64293 Darmstadt, Germany*

Abstract

In this work we present a conceptual analysis of the use of the novel Italian multibeam radar sensor BIRALES for space surveillance. The dedicated orbit determination algorithm is described in detail. The algorithm is tailored to the peculiar configuration of the receiver gain pattern and is devoted to both reconstructing the track of the object transiting in the receiver field of view and estimating its state vector. The performance of the sensor is assessed with numerical simulations, offering an analysis on both pointing strategies and orbit determination accuracy for different survey configurations.

Keywords: Initial Orbit Determination, Space Debris, Radar Sensors

1. Introduction

In the last decades, the number of man-made objects orbiting the Earth has dramatically increased. In around 60 years of space activities, more than 5450 launches have turned into around 42000 tracked objects in space, of which about

---

*Corresponding author
Email addresses:* `matteo.losacco@polimi.it` (Matteo Losacco), `pierluigi.dilizia@polimi.it` (Pierluigi Di Lizia), `mauro.massari@polimi.it` (Mauro Massari), `giovanni.naldi@inaf.it` (Giovanni Naldi), `giuseppe.pupillo@inaf.it` (Giuseppe Pupillo), `germano.bianchi@inaf.it` (Germano Bianchi), `jan.siminski@esa.int` (Jan Siminski)

23000 remain in space and are regularly tracked by the US Space Surveillance Network and maintained in their catalogue, which covers objects larger than about 5-10 cm in Low-Earth Orbit (LEO) and from 30 cm to 1 m at geostationary (GEO) altitudes. Among all these objects, only a small fraction (about 1950) are operational satellites [1]. About 24% of the catalogued objects are satellites, and about 18% are used upper stages and mission related objects. The presence of satellites and upper stages is a source of new objects itself. Since 1961, more than 500 in-orbit fragmentation events have been recorded. Among them, only a few were collisions: the vast majority of the events were explosions of orbiting satellites and upper stages. These fragmentation events are assumed to have generated a population of so called "space debris" or "orbital debris" with estimated numbers of around 34000 objects larger than 10 cm, 900 000 objects from 1 cm to 10 cm, and 128 million objects from 1 mm to 1 cm [1, 2].

The presence of space debris unavoidably jeopardizes the operative mission of active satellites. The consequences of a possible collision between an operative satellite and space debris may be the satellite failure or, in the worst case scenario, satellite destruction and fragments generation, with inevitable environmental drawbacks and possible cascade effects [3]. This hazard calls for the crucial adoption of countermeasures aiming at reducing mission related risks. Specific space programmes were started to build the expertise required to manage the challenges posed by the space traffic control problem. Collision risk assessment is performed daily by satellite operators who are provided with conjunction data messages to support decisions on the execution of collision avoidance manoeuvres [4]. In addition, re-entry predictions of objects are regularly produced to estimate on ground risks [5]. Both collision risk assessment and re-entry predictions rely on the accurate estimation and prediction of the state of the orbiting objects, which are derived from tracking actions by dedicated optical, radar and laser sensors.

Survey and tracking of objects in Earth orbit is among the areas covered by the European Space Surveillance and Tracking (SST) Support Framework [6] and the European Space Agency (ESA) Space Situational Awareness (SSA) [7]
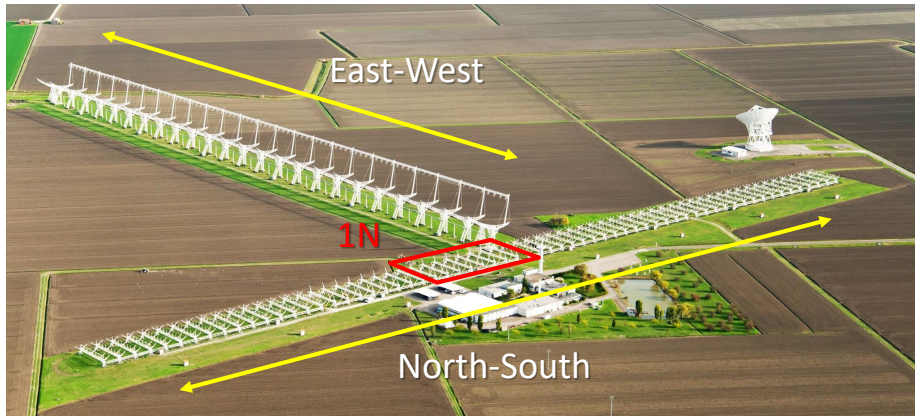
Figure 1: Medicina Northern Cross Radio Telescope.

programmes, and the setup of a European network of sensors is one of their main objectives. This paper investigates the role of the novel Italian multi-beam BIstatic RAdar for LEo Survey (BIRALES) within the European framework [8, 9]. BIRALES couples two different radar systems to simultaneously obtain Doppler shift and slant range measurements. The main characteristic of the sensor is represented by the possibility of reconstructing the track of the transiting object in the receiver field of view (FoV) by processing the data acquired by a set of electronically formed beams. This operation is hindered by the complicated gain pattern of the antenna, and a suitable algorithm for track reconstruction is required. The resulting angular profiles, coupled with the measured slant range and Doppler shift values, enable initial orbit determination (IOD) with a single passage of the object in the sensor FoV.

The paper is organized as follows. After describing the sensor architecture, the first part of the paper illustrates the dedicated IOD algorithm. The second part of the work offers an analysis of the performance of the sensor, in terms of both observation capabilities and orbit determination accuracy. All the analyses and examples presented in the paper are obtained with numerical simulations.
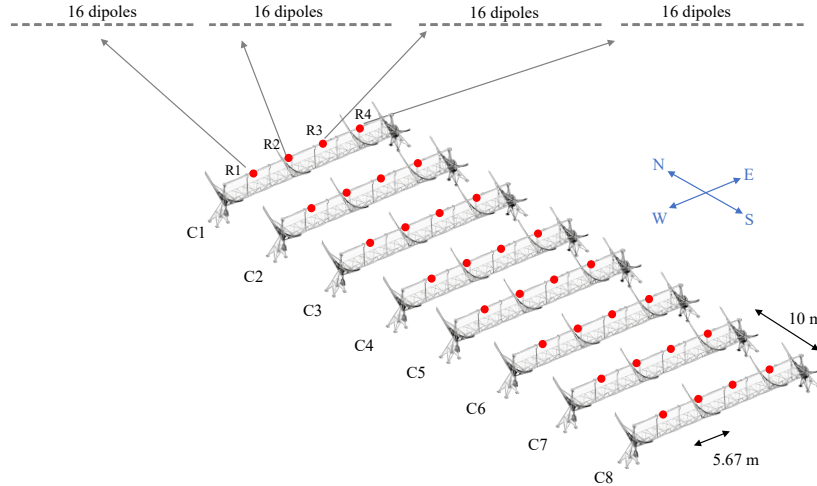
3

Figure 2: BIRALES 1N-section scheme. The system consists of 8 cylindrical parabolic reflectors (C). Four receivers (R) are located along the focal line of each cylinder. Each receiver is connected to 16 dipoles.

2. BIRALES sensor

BIRALES is an Italian radar sensor with a bistatic configuration. The "Radio Frequency Transmitter" (RFT) located at the Italian Joint Test Range of Salto di Quirra (PISQ) in Sardegna is used as transmitter (TX), and the Northern Cross radio telescope of the radio astronomy station of Medicina (Bologna, Italy) as receiver (RX). The RFT (longitude 9° 26' 23", latitude 39° 36' 18", altitude 684.73 m) has a powerful amplifier able to supply a maximum power of 10 kW in the bandwidth 410-415 MHz. It is a 7 m dish steerable at a maximum speed of 3 deg/s with right-hand circular polarization and a beamwidth of 7 deg. The receiving antenna is a portion of the Northern Cross radio telescope, which is currently one of the largest UHF-capable antennas in the world. The overall system consists of two perpendicular branches (see Fig. 1): the East-West (E-W) arm is 564 m long and is made of a single 35 m wide cylindrical antenna, whereas the North-South (N-S) branch is made of 64 parallel antennas with a length of 23.5 m and width of 7.5 m each. The portion dedicated to BIRALES

4

receiving antenna is called "1N-section" (longitude 11° 38' 45", latitude 44° 31' 27", altitude 28.0 m). The "1N-section" is an array composed of 8 cylindrical

70 parabolic concentrators belonging to the N-S arm (see Fig. 2). In the focal line (aligned with the E-W direction), each cylinder contains four receivers. The receiving system, therefore, is composed of a matrix of 8 x 4 receivers spaced 5.67 m in E-W ($d_{\text{E-W}}$) and 10 m in N-S ($d_{\text{N-S}}$). The 8 cylinders can be mechanically pointed only in elevation (El_{RX}) along the local meridian. The mechanical ele-

75 vation limits are 22.5 deg $\leq El_{\text{RX}} \leq$ 90 deg in North pointing configuration and 17.0 deg $\leq El_{\text{RX}} \leq$ 90 deg in South pointing configuration. This mechanical pointing involves all the array elements (receivers).

BIRALES exploits at the same time two different systems:

- Multibeam Continuous-Wave (CW) unmodulated radar

80 - Single-beam pulse compression radar

The first system has the purpose of measuring the Doppler shift and the angular profiles of the target, while the second system, which is a recent upgrade for BIRALES, provides the slant range measurements. The total power budget of the overall system is 10 kW, and it is equally divided between the CW and the

85 pulse signals. A scheme of the signal processing is given in Fig. 3, whereas a detailed description of the two systems is provided hereafter.

2.1. Multibeam unmodulated CW radar

The multibeam unmodulated CW system has the purpose of providing Doppler shift measurements and multiple SNR profiles which are later used in the multi-

90 beam orbit determination algorithm (see Section 3). The RFT radiates a CW unmodulated signal at the frequency of 410.085 MHz. When an orbiting object is illuminated by the radiated signal and falls in the RX FoV, the radio echo is received by the Northern Cross. The total bandwidth of the receiving system is 16 MHz, centred at 408 MHz. Each cylinder of the "1N-section" is characterized

95 by a feed consisting of 64 dipoles placed along the focal line. The four receivers combine the dipole signals in groups of 16, resulting in 4 analogue channels
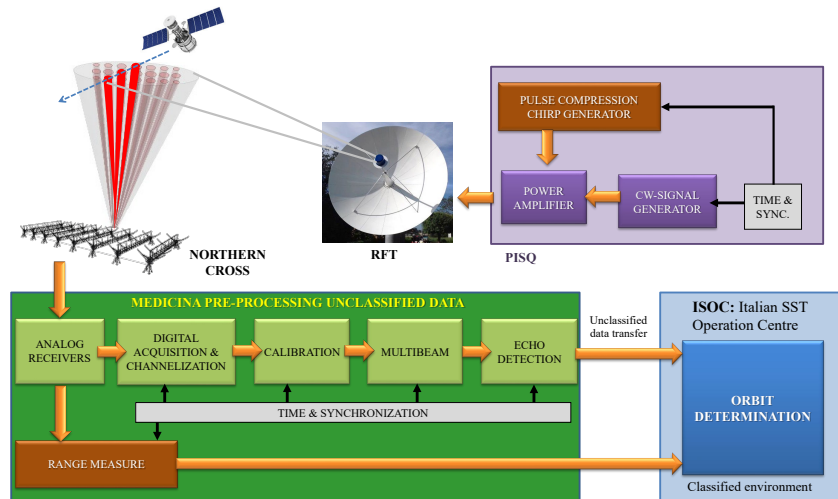
5

Figure 3: BIRALES signal processing block diagram. The RX and TX are synchronized by a GPS clock system, granting a maximum error of 10^{-7}s.

per cylinder. The amplified signals travel to a RX room through 520 m long optical fiber links [10], and here they are down-converted to the intermediate frequency of 30 MHz and then fed to a digital back end. The back end digitalizes and channelizes the signals into a total of 256 coarse frequency channels of 78.125 kHz bandwidth, each. The channelization is done using a Polyphase Filter Bank (PFB) processing technique [11]. The channelized signals are then transmitted to a server over a 10 Gb Ethernet link. The transmitted data are expressed in a 32-32 complex fixed point format, and they are translated into a floating point format using the Data AcQuisition library developed for the Aperture Array Verification System of the SKA LFAA (Square Kilometre Array - Low Frequency Aperture Array) project (AAVS DAQ). The 32-input stream thus generated is then fed to a beamformer module. Here each signal is delayed in the frequency domain by applying a phase correction to each individual channel in order to point the beam in the desired direction. Signals are also corrected using instrumental gain and phase to compensate differences in electronic chains; then they are summed together channel by channel to form
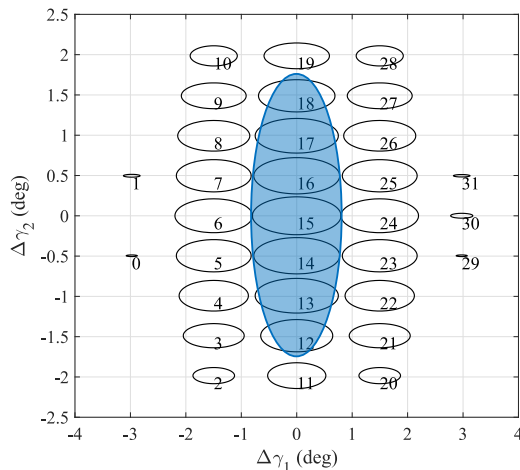
6

Figure 4: BIRALES RX multibeam configuration (elevation 90 deg) as a function of the angular deviations $\Delta\gamma_1$ and $\Delta\gamma_2$ with respect to the RX pointing direction. Contours define the -3 dB beamwidth of each beam main lobe with respect to the RX main lobe maximum gain. In blue, the single analogue beam of the pulse compression radar system.

the beams. Once generated, all the electronically formed beams are kept fixed (no tracking corrections are applied to the steering vector) in the FoV. In the current configuration, a 32-beam configuration is used (see Fig. 4).

After the beamforming, fine channelization is performed, splitting the original coarse channel into 8192 separate channels of $\sim$9.5 Hz, thus granting a temporal resolution of about 0.1 s. This operation is done using the PFB technique previously mentioned. The beamformed data are then sent to the detection module. The detection module analyses the beamformed data in order to extract potential space debris candidates. The analysis is performed in different phases. A pre-processing module receives the channelized data and computes the power P from the received antenna voltages V. Then, the system progressively filters out the noise. First, background noise is eliminated. Then, a binary hit-or-miss transform is used to eliminate random and isolated pixels with high SNR. The filtered data are then further analysed by the detection module. The system developed for BIRALES uses a Density-Based Spatial Clustering of

7

Applications with Noise (DBSCAN) method [12]. The algorithm groups data points based on their proximity to each other, thus generating clusters. Clusters belonging to the same object are merged using a tracklet linking algorithm. In the end, the data associated with a single detection are collected in a Tracking Data Message (TDM) file [13]. The TDM file contains, for all the illuminated beams, the illumination instants, and the corresponding measured Signal-to-Noise Ratio (SNR) and Doppler shift (DS). The SNR measured by a specific beam i is the ratio between the received signal power and the noise power [14]:

$$SNR^i = 10 \log_{10} \left(\frac{P_{\mathrm{RX}}^i}{N^i} \right) \tag{1}$$

with

$$P_{\mathrm{RX}}^i = \frac{P_{\mathrm{TX}} \cdot G_{\mathrm{TX}} \cdot G_{\mathrm{RX}}^i \cdot RCS \cdot \lambda^2}{(4\pi)^3 \rho_{\mathrm{sat\text{-}TX}}^2 \cdot \rho_{\mathrm{sat\text{-}RX}}^2} \tag{2}$$

where P_{TX} is the power radiated by the TX, G_{TX} the gain of the TX antenna, G_{RX}^i the gain of the single beam of the RX, RCS the radar cross section of the transiting object, λ the wavelength of the signal, $\rho_{\mathrm{sat\text{-}TX}}$ the distance between the TX and the object, and $\rho_{\mathrm{sat\text{-}RX}}$ the distance between the RX and the object, whereas N^i is the measured noise level.

Doppler shift measurements are obtained by measuring the received frequency and then comparing this frequency with the known transmitted CW unmodulated signal. If the value of SNR is larger than an imposed threshold (typically 6 dB), the values of time instant, SNR and Doppler shift are recorded.

In some cases, one may observe the presence of isolated clusters that are clearly false positives. False positives are handled by a validation process, which consists in analysing the clusters according to the number of associated data points, their Doppler shift and rate of change of the Doppler itself, and discarding the ones with unrealistic values. In the current parameter setup, the percentage of false alarms detected during the first measurements campaigns is about 1%. A more detailed analysis about the detection module can be found in [15].

2.2. Single-beam pulse compression radar

While transmitting the CW unmodulated signal, the RFT simultaneously radiates a pulsed chirp signal with about 4 MHz bandwidth, centred at 412.5 MHz, and a Pulse Repetition Frequency (PRF) of around 70 Hz, selected to observe targets at a maximum range of 2000 km. To obtain a proper SNR at the RX, the duration of the uncompressed pulse ranges from 200 to 500 ms. The duration of the compressed pulse, instead, is selected in order to achieve a desired range resolution of 30 m, and it is equal to 200 ns [16]. The radiated signals, when reflected by the transiting object, are collected by 128 dipoles distributed among 2 adjacent cylinders of the Northern Cross, and then sent by means of optical fiber links to an analogue beamformer. The beamformer generates a single analog beam, which at present covers just a portion of the FoV of the multibeam system (see Fig. 4, blue beam). The processed signal is then converted to an intermediate frequency of 30 MHz, and sent to the ranging measurement module. Here the signal is digitalized and sent to a pulse compressor, where a matched filter is used. The resulting signals are then analysed by a Coherent Integrator. The Integrator samples and adds the signals returning from each of the N transmitted pulses at a spacing equal to the resolution of the radar. After accumulating the N pulses, it performs the amplitude detection and threshold check, and generates a Doppler-slant range map. This map is analysed by an Extractor module, which identifies possible individual targets in the map. Constant False Alarm Rate (CFAR) methods are used to set a constant a priori probability of false alarms [17]. Further details about the ranging system architecture can be found in [16].

In the end, the system provides, for each identified target, different observation epochs and the corresponding slant range (SR) measurements. A data fusion algorithm assembles the measurements gathered simultaneously by the two radar systems: this guarantees the generation of a single TDM file, in which the single-beam slant range measurements are attached to the multibeam Doppler shift and SNR measurements. Given the different FoV of the two receiving systems, slant range measurements obtained with the pulse compression radar

9

and Doppler shift measurements provided by the multibeam CW unmodulated
radar are obtained at different time epochs, i.e. slant range measurements are
available just for a portion of the passage of the transiting object. Before per-
forming IOD, an extrapolation of slant range data is performed, so that, for
each illumination instant, both Doppler shift and slant range measurements are
available. For the analyses and examples shown in this paper, an upgrade of
the sensor, with the single beam covering the whole multibeam FoV, will be
considered. In the end, the collected time instants, Doppler shift and slant
range measurements, along with the SNR profiles measured by the multibeam
system, represent the input for the Multibeam Orbit Determination Algorithm
(MODA).

3. Multibeam Orbit Determination Algorithm

The IOD strategy developed for BIRALES processes the data contained in
the TDM file to estimate the orbital elements of the detected object. The
algorithm works in two steps. The first step is dedicated to the estimation
of the angular path, or track, of the object in the RX FoV starting from the
available SNR profiles measured by the multibeam system and the slant range
measurements. The second step focuses on the object state estimation on the
basis of the first-step estimated track, and the available slant range and Doppler
shift measurements. Both steps are described in detail in the following sections.

3.1. Track reconstruction

The beam illumination sequence provided by the multibeam system offers
in principle the possibility of identifying the track followed by the object while
transiting in the RX FoV, thus adding an angular information to the already
available slant range and Doppler shift measurements. Nevertheless, the anal-
ysis of the detected signal must account for the complex gain pattern of the
multibeam RX, which is different for each beam and changes with the RX el-
evation. Figure 4 shows the distribution of the 32 beams in the RX FoV. The
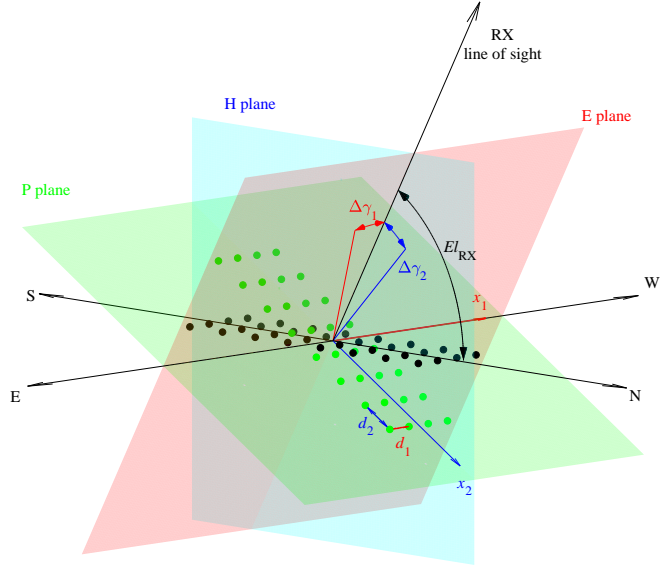
10

Figure 5: Reference system for BIRALES RX array and beam characterization. Black dots show the physical location of the 32 receivers, green dots their projection onto the P plane.

angles $\Delta\gamma_1$ and $\Delta\gamma_2$ are the angular deviations with respect to the RX pointing direction. The angle $\Delta\gamma_2$ is defined on the H-plane, which for BIRALES coincides with a plane that is normal to the azimuth plane and includes the N-S direction, whereas $\Delta\gamma_1$ is measured on the E-plane, which includes the RX pointing direction and intersects the azimuth plane along the E-W direction (see Fig. 5). The plotted contours represent the -3 dB beamwidth of the beam main lobe with respect to the maximum gain of the RX main lobe.

Along with the main lobes, the geometry of the receivers distribution is responsible for the generation of additional lobes, called grating lobes, whose size is tapered by the element pattern shape. Grating lobes appear when the spacing between the receivers is larger than $\lambda/2$, where λ is the wavelength of the radiated signal [18]. The actual spacing of the receivers as seen by the incoming wavefront must be computed by projecting the 32 receivers distribution onto a plane normal the direction of the incoming signal. Given the small FoV of

11

the RX, we can assume that this direction is almost coincident with the RX pointing direction, therefore the projection plane intersects the azimuth plane along he E-W direction. We will define this plane as P plane. A sketch of the geometry of the array is given in Fig. 5 (El_{RX} 60 deg, North pointing): black dots represent the physical location of the receivers, green dots their projection onto the P plane. Two directions can be identified on the P plane: a first direction x_1, which is coincident with the E-W axis, and a second direction x_2, which is the projection of the N-S direction onto the P plane. The spacing of the receivers along x_1, here defined d_1, governs the angular separation of the grating lobes in the $\Delta\gamma_1$ direction, and is always equal to $d_{E\text{-}W}$, regardless of the RX mechanical elevation. The spacing d_2 of the receivers along x_2, instead, governs the angular separation of the grating lobes in the $\Delta\gamma_2$ direction and it decreases with the RX elevation, i.e. $d_2 = d_{N\text{-}S}\sin(El_{RX})$. Once defined d_1 and d_2, the angular separation of the grating lobes from each single beam main lobe can be expressed as

$$\Phi^m_{\Delta\gamma_i} = \operatorname{asin}\left(\frac{m}{d_{i,\lambda}}\right) \tag{3}$$

where i indicates one of the two directions, m is the grating lobe index (1,2,3,...), $d_{i,\lambda}$ is the spacing of the receivers in the x_i direction in multiples of the wavelength λ, whereas $\Phi^m_{\Delta\gamma_i}$ is the angular distance of the grating lobe m from the beam main lobe in the $\Delta\gamma_i$ direction.

Let us analyse what happens in nadir-pointing configuration. In this case, the spacing of the receivers in the two directions d_1 and d_2 coincides with the physical spacing along the E-W and N-S directions, and it is equal to 7.75λ and 13.68λ, respectively. Both spacings are larger than $\lambda/2$, therefore grating lobes appear in both directions. If we rely on Eq. 3, we obtain that $\Phi^1_{\Delta\gamma_1} \sim 7.4$ deg and $\Phi^1_{\Delta\gamma_2} \sim 4.2$ deg.

The magnitude of each beam main lobe and grating lobes is governed by the tapering action of the element pattern shape, which progressively attenuates the lobes while moving towards the boundaries of the RX FoV. As a result, beams that are located at the boundaries of the FoV have a weaker main lobe

12

with respect to beams close to the RX line of sight. On the other hand, the relevance of the grating lobes in the two angular directions mainly depends on the position of the beam main lobe in the FoV. Beams that are located close to the RX line of sight (e.g. beam 15 or beam 24) typically show grating lobes in the $\Delta\gamma_2$ direction with a much lower gain with respect to the main lobe, whereas grating lobes in the $\Delta\gamma_1$ direction do not appear, as, at a distance of at least 7 deg from the beam main lobe, the element pattern shape has already reduced them to very low values. Figure 6a shows a contour plot of the gain pattern of beam 15 at an elevation of 90 deg. The represented gain is the relative gain with respect to the maximum gain of the RX, which corresponds to the gain peak of the main lobe of beam 15. Contour lines are plotted from -1 dB to -111 dB, with a spacing of 10 dB. The region inside each contour line is coloured according to the gain level of the line itself. As can be seen, the beam has its main lobe at ($\Delta\gamma_1$=0 deg; $\Delta\gamma_2$=0 deg), and its level is obviously equal to 0 dB. All around the main lobe, we can distinguish several side lobes, and two grating lobes in the $\Delta\gamma_2$ direction, located at ($\Delta\gamma_1$=0 deg; $\Delta\gamma_2$=4.15 deg) and ($\Delta\gamma_1$=0 deg; $\Delta\gamma_2$=-4.15 deg), with relative gain equal to -7.72 dB and -8.3 dB, respectively. That is, the largest grating lobe is a factor 6 weaker than the beam main lobe. On the contrary, beams that are far from the RX line of sight generally show at least one grating lobe whose gain peak is comparable with the one of the main lobe. Figure 6c shows the gain pattern of beam 20 at an elevation of 90 deg: the main lobe, located at ($\Delta\gamma_1$=1.50 deg; $\Delta\gamma_2$=-1.99 deg), and the grating lobe, located at ($\Delta\gamma_1$=1.50 deg; $\Delta\gamma_2$=2.18 deg), have similar gain peaks (-2.38 dB and -2.51 dB respectively). Also in this case, the grating lobes in the $\Delta\gamma_1$ direction are not relevant.

As previously described, the gain pattern is further affected by the RX elevation: as the elevation decreases, the spacing of the receivers in the x_2 direction decreases, and so, for each single beam, the main lobe position tends to remain unaltered, while the grating lobes in the $\Delta\gamma_2$ direction progressively move away from the main lobe, thus reducing their size. Furthermore, the shape of the lobes changes, with both main lobe and grating lobes enlarging in the $\Delta\gamma_2$ di-
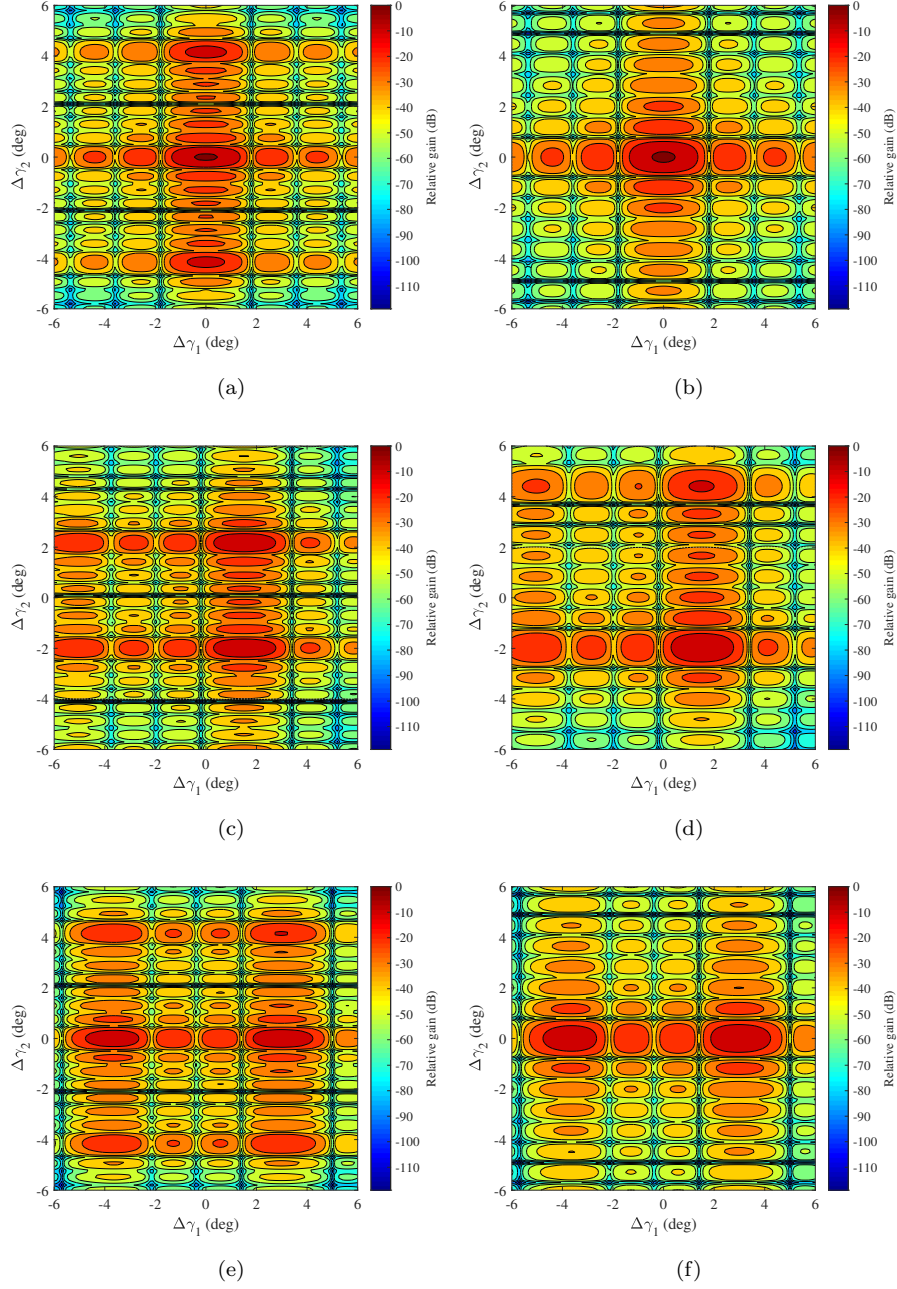
13

Figure 6: BIRALES RX gain pattern dependency on beam position and RX elevation: beam 15, (a) 90 deg and (b) 40 deg elevation, beam 20, (c) 90 deg and (d) 40 deg elevation, beam 30, (e) 90 deg and (f) 40 deg elevation. The plotted gain is the relative gain with respect to the maximum gain of beam 15. Contour lines are plotted from -1 dB to -111 dB, with a spacing of 10 dB.
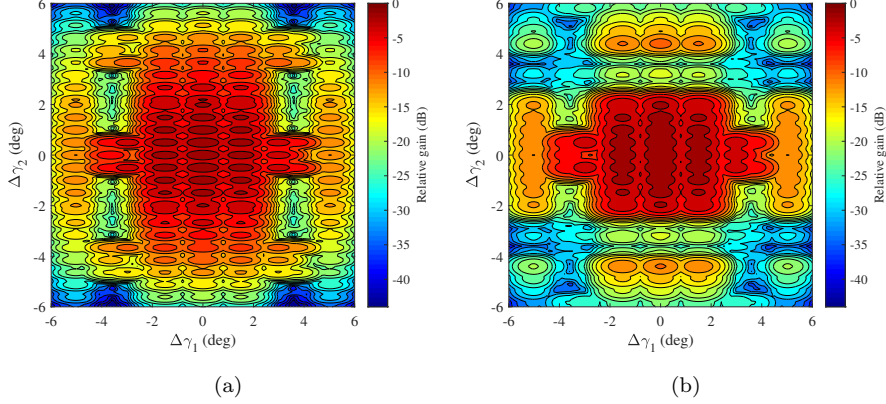
14

Figure 7: BIRALES overall RX gain pattern dependency on elevation: (a), 90 deg, (b), 40 deg. The plotted gain is the relative gain with respect to the maximum gain of beam 15. Contour lines are plotted from -1 dB to -44 dB, with a spacing of 2 dB.

rection. An example is reported in Figs. 6b and 6d, which show the gain pattern
of beams 15 and 20 at 40 deg elevation.

The grating lobes in the $\Delta\gamma_1$ direction appear only for beams that are located at the boundaries of the RX FoV in that direction. Figure 6e shows the gain pattern distribution for beam 30. The main lobe is located at ($\Delta\gamma_1$=2.98 deg; $\Delta\gamma_2$=0 deg), and it shows a relative gain peak equal to -2.87 dB. Unlike the previous cases, grating lobes now appear in both directions. The largest grating lobe is located at ($\Delta\gamma_1$=-3.64 deg; $\Delta\gamma_2$=0 deg), and its relative gain peak is -4.48 dB. Other two grating lobes can be identified in the $\Delta\gamma_2$ direction (($\Delta\gamma_1$=2.98 deg; $\Delta\gamma_2$=4.15 deg) and ($\Delta\gamma_1$=2.98 deg; $\Delta\gamma_2$=-4.15 deg), respectively), though their relative gain peak is comparable with the one of some side lobes (-10.59 dB, -11.16 dB). As the elevation decreases, the main lobe and the first grating lobe do not move, as the spacing of the receivers in the x_1 direction is not affected by the RX elevation, whereas the two grating lobes along $\Delta\gamma_2$ move away and disappear (see Fig. 6f).

The contribution of all the beams brings about a complicated RX gain pattern. The overall gain pattern at 90 deg and 40 deg of elevation is shown in
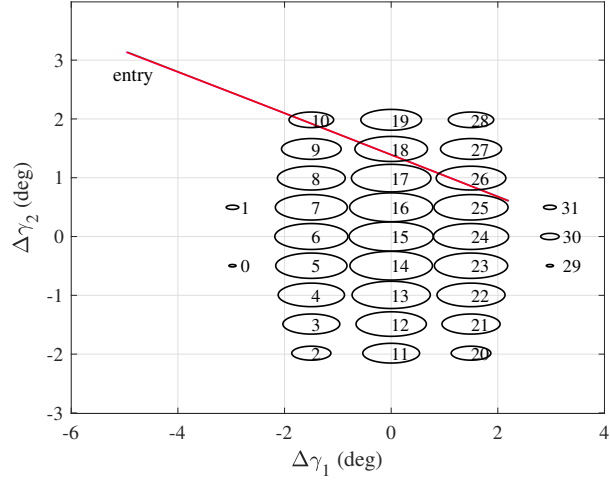
(a)
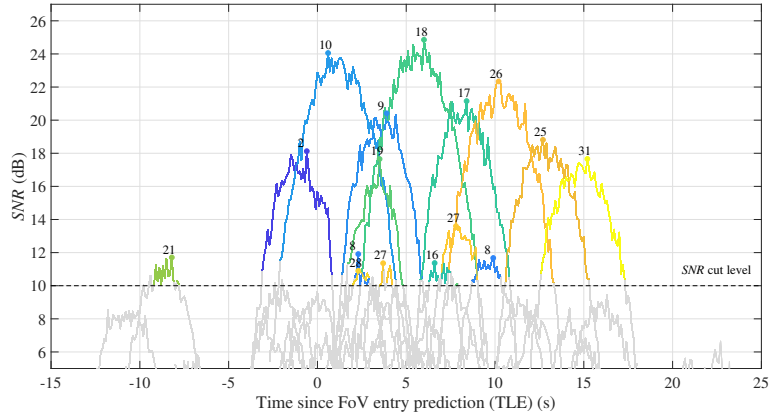
(b)

Figure 8: BIRALES RX beam illumination example (object NORAD ID 00446, passage epoch 19 DEC 2018 08:46:47.943 UTC, El_RX 70 deg, North pointing, El_TX 48.97 deg, Az_TX 9.40 deg): (a), real track of the object; (b), pre-filtered SNR profile and SNR peaks as a function of the time difference between the real passage epoch and the predicted entry epoch in the RX FoV. Different colors are used for the different beams. For each beam, the maximum signal peak and beam identification number are reported.

Fig. 7. The resulting gain pattern unavoidably complicates the analysis of the received signal, and makes the reconstruction of the object track a non trivial task. Every time a beam is illuminated, it is not straightforward to identify the gain lobe responsible for the beam illumination. This is particularly true when the sensor is used in survey mode, with observed objects that may be uncatalogued and may transit at the boundaries of the FoV, illuminating both the grating lobes of the central beams and the main lobes of the peripheral ones. In principle, for each illuminated beam, multiple gain lobe candidates exist, and the number of possible combinations increases with the number of illuminated beams. Conversely, only one solution is compliant with the measured SNR profile. An example is shown in Fig. 8, for object NORAD ID 00446 (passage epoch 19 DEC 2018 08:46:47.943 UTC, El_{RX} 70 deg, North pointing): at the top, the passage of the transiting object in the RX FoV; at the bottom, the generated SNR profile. As can be seen, both main lobes (beams 10, 9, 18, etc.) and grating lobes (beams 21, 2, 28, etc.) contribute to the overall SNR profile.

The track reconstruction phase starts from the detected signal, and tries to reconstruct the angular path in time $\boldsymbol{u}(t) = (\Delta\gamma_1(t), \Delta\gamma_2(t))^{\mathrm{T}}$ in the RX FoV taking into account the presence of multiple gain lobes per beam. Two different phases can be identified: a *filtering phase*, in which possible candidates for the object track are identified, and a *refinement phase*, in which the best candidate is selected. A scheme for the track reconstruction algorithm is shown in Fig 9. A detailed description of the two phases is provided hereafter.

3.1.1. Filtering phase

The track reconstruction algorithm starts from the analysis of the detected SNR profile for all the illuminated beams. The number of illuminated beams depends on the RCS and the slant range of the transiting object. Before estimating the object track, the detected signal is cut to consider only a desired number of illuminated beams. The cut is done by selecting a number of illuminated beams n_{sel}, and reducing the SNR profile so that the final number of illuminated beams $n_{\mathrm{ill}} \leq n_{\mathrm{sel}}$. An example is shown in Fig. 8b: in grey,
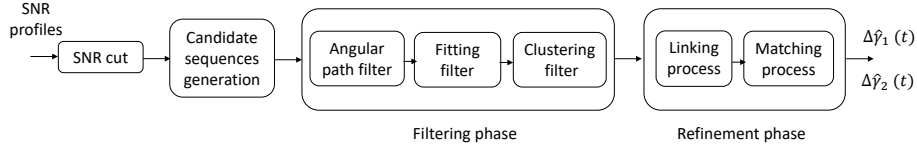
17

Figure 9: Track reconstruction algorithm.

the portion of the SNR profile discarded, in color, the pre-filtered SNR. This procedure is optional and aims at speeding up convergence when the number of illuminated beams is large. An analysis of the impact of the number of considered beams on the IOD accuracy is presented in Section 4.

295   Starting from the obtained pre-filtered SNR profile, the *filtering phase* aims at generating possible first guesses for the object track by identifying realistic gain peak sequences (here called "candidate sequences") that are compliant with the measured SNR peak sequence. The generation of the candidate sequences starts considering a subset of illuminated beams $n_{\mathrm{filt}} = \min\{10, n_{\mathrm{ill}}\}$, and iden-

300   tifying for each beam i its maximum measured SNR peak s^i. In principle, each SNR peak s^i may be associated with any of the gain peaks p_j^i of that beam, where the gain peaks include main lobe, grating lobes and side lobes, and are here sorted in descending order of gain value g_j^i. For each beam, the first n_{peaks} gain peaks are considered, with $n_{\mathrm{peaks}} = \{2, 3, 4\}$, and candidate sequences are

305   generated by computing all the possible combinations of the selected gain peaks.

     Let us consider the passage shown in Fig. 8. The analysis of the SNR profile gives the following SNR peak sequence:

$$\boldsymbol{s} = \left(s^2, s^{10}, s^{19}, s^9, s^{18}, s^{27}, s^{17}, s^{26}, s^{25}, s^{31}\right)^{\mathrm{T}}$$

where the superscripts indicate the beam identification number. The candidate gain peak sequences are obtained by associating each SNR peak s^i to one of the first n_{peaks} gain peaks of its beam. The following sequences are therefore

18

obtained:

$$\left(p_1^2, p_1^{10}, p_1^{19}, p_1^9, p_1^{18}, p^{27}, p_1^{17}, p_1^{26}, p_1^{25}, p_1^{31}\right)^{\mathrm{T}}$$

$$\left(p_2^2, p_1^{10}, p_1^{19}, p_1^9, p_1^{18}, p^{27}, p_1^{17}, p_1^{26}, p_1^{25}, p_1^{31}\right)^{\mathrm{T}}$$

$$\left(p_1^2, p_2^{10}, p_1^{19}, p_1^9, p_1^{18}, p^{27}, p_1^{17}, p_1^{26}, p_1^{25}, p_1^{31}\right)^{\mathrm{T}}$$

$$\vdots$$

For the case under study, with $n_{\mathrm{filt}} = 10$ and $n_{\mathrm{peaks}} = 2$, 1027 possible candidate sequences are identified. As the number of considered beams and gain peaks increases, the number of candidate sequences drastically increases. Thus, a trade-off between the number of considered beams and gain peaks must be performed.

Among the generated sequences, some are realistic, others identify unfeasible angular paths in the RX FoV. In order to reduce the number of candidates, the generated sequences go through different filters that aim at identifying the most realistic ones. The first filter consists in computing, for all the generated candidates, their angular path length L in the RX FoV. Given a generic gain peak p_j^i, its position in the RX FoV is identified by the vector $\tilde{\boldsymbol{u}}_j^i = (\Delta\gamma_1, \Delta\gamma_2)_j^{i\ \mathrm{T}}$. For each generated candidate sequence, the angular path length L is computed as:

$$L = \sum_{i=1}^{n_{\mathrm{filt}}-1} ||\tilde{\boldsymbol{u}}_{J(i+1)}^{I(i+1)} - \tilde{\boldsymbol{u}}_{J(i)}^{I(i)}|| \tag{4}$$

where I is the vector of the selected beams, whereas J is the vector of gain peak indexes of the candidate sequence. For the example considered, $I = (2, 10, 19, 9, 18, 27, 17, 26, 25, 31)^{\mathrm{T}}$, whereas J is specific to each sequence, i.e.

$$(1, 1, 1, 1, 1, 1, 1, 1, 1, 1)^{\mathrm{T}}$$

$$(2, 1, 1, 1, 1, 1, 1, 1, 1, 1)^{\mathrm{T}}$$

$$(1, 2, 1, 1, 1, 1, 1, 1, 1, 1)^{\mathrm{T}}$$

$$\vdots$$

Good candidate sequences must have low angular displacements between two consecutive gain peaks. The sequences are sorted in ascending order according

19

to their performance value L, a first ranking is obtained, and only sequences with a value of $L < 1.5\,d$, with d equal to the length of the diagonal of the RX FoV, are accepted. This initial filter prunes away unrealistic gain peak sequences.

The filtering action based on the angular path length criterion, however, is not sufficient. Especially when considering a value of $n_{\mathrm{peaks}} > 2$, the first filtering action may reward sequences with gain peaks very close one to the others, and may penalize other sequences that have more spatially distributed peaks. For this reason, a second filtering action is applied to sequences that pass the first filter. The angular path in the RX FoV is approximated with a linear regression in time

$$\boldsymbol{u}(t) = \bar{\boldsymbol{u}} + (t - t_0)\dot{\boldsymbol{u}} \tag{5}$$

where t_0 is the epoch of the first observation. Knowing the epoch t^i at which each signal peak s^i is measured, each candidate sequence undergoes a linear fit expressed as

$$\min_{\bar{\boldsymbol{u}},\dot{\boldsymbol{u}}} \sum_{i=1}^{n_{\mathrm{filt}}} \left[\tilde{\boldsymbol{u}}_{J(i)}^{I(i)} - \boldsymbol{u}\left(t^{I(i)}\right) \right]^{\mathrm{T}} \left[\tilde{\boldsymbol{u}}_{J(i)}^{I(i)} - \boldsymbol{u}\left(t^{I(i)}\right) \right] \tag{6}$$

For each candidate sequence, the solution of Eq. 6 provides a value of residual R, and the estimates for the linear regression parameters $\widehat{\bar{\boldsymbol{u}}}$ and $\widehat{\dot{\boldsymbol{u}}}$. This second filtering action introduces the time variable in the selection of the candidates. All the sequences are sorted in ascending order according to their value of R, and a new ranking is obtained. Generally, the top entries of the new ranking are very similar and tend to differ by only a couple of elements in the corresponding sequences. In order to identify sequences that cover different regions of the FoV of the sensor, the candidate sequences are finally divided into clusters, and the first n_{sol} (two or three) solutions are identified. The selected sequences are the final candidates that pass to the second phase, the *refinement phase*, and each of them is now associated with an estimate of the object track, i.e.

$$\widehat{\boldsymbol{u}}(t) = (\Delta\widehat{\gamma}_1(t), \Delta\widehat{\gamma}_2(t))^{\mathrm{T}} = \widehat{\bar{\boldsymbol{u}}}_{\mathrm{f}} + (t - t_0)\widehat{\dot{\boldsymbol{u}}}_{\mathrm{f}} \tag{7}$$

20

with $t \in T_{\mathrm{ill}}$, T_{ill} vector of all the illumination instants, whereas the subscript "f" indicates that the estimate is obtained during the *filtering phase*.

3.1.2. Refinement phase

320   The candidate sequences selected by the filtering process are obtained considering a subset of illuminated beams, and their maximum signal peaks $\boldsymbol{s}$ only. The best candidate sequence is identified in the *refinement phase*, in which all the illuminated beams and their whole SNR profile are considered. Figure 10 illustrates the workflow of the track reconstruction for the best candidate se-
325 quence of the passage shown in Fig. 8. The real passage of the object is reported in red.

For each single candidate sequence, the *refinement phase* starts from the estimated object track obtained during the *filtering phase* (see Eq. 7). This estimate was obtained considering only a subset of n_{filt} beams, and only the maximum signal peak for each beam. If we consider Fig. 10a, the black line represents the estimated object track obtained during the *filtering phase* for the best candidate sequence. Black dots indicate the position of the gain peaks used to obtain this estimate, with numbers showing the beam they refer to. Before considering the whole SNR profile of each beam, the linear fit is refined in an intermediate step, here defined *linking process*. The basic idea of the *linking process* is to consider all the illuminated beams and measured SNR peaks $\boldsymbol{S}$, with $\boldsymbol{S} \in \mathbb{R}^{n_{SNR}}$, n_{SNR} overall number of SNR peaks, and associate each signal peak of a beam with a given gain peak of the same beam. If we recall the example shown in Fig. 8, the SNR peak sequence now becomes:

$$\boldsymbol{S} = \big(S^{21,1}, S^{2,1}, S^{10,1}, S^{8,1}, S^{28,1}, S^{27,1}, S^{19,1}, S^{9,1}$$
$$S^{18,1}, S^{16,1}, S^{27,2}, S^{17,1}, S^{8,2}, S^{26,1}, S^{25,1}, S^{31,1}\big)^{\mathrm{T}} = \big\{S^{k,v}\big\}^{\mathrm{T}}$$

In the notation, the superscript v indicates the SNR peak number. For example, $S^{8,1}$ indicates the first SNR peak for beam 8, $S^{8,2}$ its second SNR peak and so on. The *linking process* relies on the available estimate of the object track, i.e.
330 the one obtained during the *filtering phase* (black line). For each illuminated
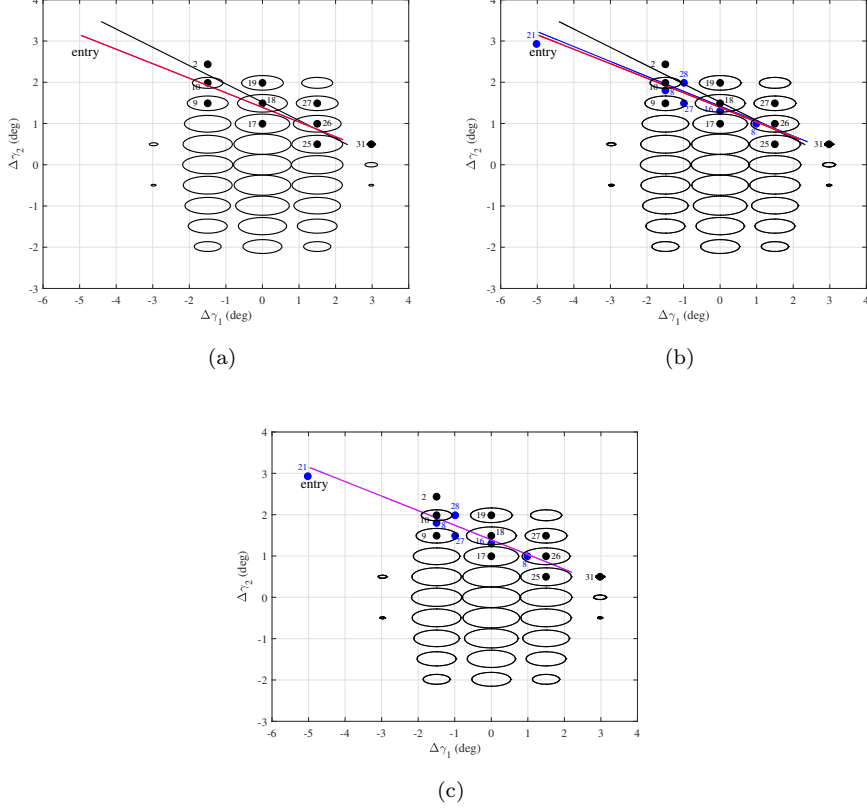
21

Figure 10: Track reconstruction process for the best candidate sequence (object NORAD ID 00446, passage epoch 19 DEC 2018 08:46:47.943 UTC, El_{RX} 70 deg, North pointing, El_{TX} 48.97 deg, Az_{TX} 9.40 deg): (a), first guess definition based on the main SNR peaks of the first n_{filt} beams (black); (b), *linking process* performed considering all SNR peaks (blue); (c), *matching process* and estimated track (magenta) (1σ SR noise level of 10 m, 1σ SNR fluctuation level of 0.2 dB, n_{sel} equal to 13).

beam, the procedure is the following:

1. Consider a single signal peak $S^{k,v}$ and the associated time epoch $t^{k,v}$.

2. Use Eq. 7 to estimate the angular position of the object at time epoch $t^{k,v}$

$$\widehat{\boldsymbol{u}}(t^{k,v}) = \left(\Delta\widehat{\gamma}_1(t^{k,v}), \Delta\widehat{\gamma}_2(t^{k,v})\right)^{\text{T}} = \widehat{\overline{\boldsymbol{u}}}_{\text{f}} + (t^{k,v} - t_0)\widehat{\dot{\boldsymbol{u}}}_{\text{f}} \qquad (8)$$

3. Compute the angular distance $L_n^{k,v}$ from each single gain peak of the beam.

22

For this phase, the first 20 gain peaks are considered.

$$L_n^{k,v} = ||\tilde{\boldsymbol{u}}_n^k - \widehat{\boldsymbol{u}}(t^{k,v})|| \qquad n = 1, \ldots, 20 \tag{9}$$

4. Sort the results in ascending order according to the angular distance value $L_n^{k,v}$.

5. Repeat the procedure for all the SNR peaks of the beam.

The above procedure provides, for each SNR peak of a given beam, a ranking of possible associated gain peaks. The SNR peaks are then sorted in descending order of SNR value, the first signal peak is associated with the first gain peak of its ranking list, and a univocal association between signal and gain peak is thus performed for all the detected SNR peaks, scanning their ranking and selecting the first available gain peak.

This procedure is repeated for all the illuminated beams. At the end of the *linking process*, all measured SNR peaks of all the beams are associated with a given gain peak. Let us define with K and V the lists of beam and SNR peak numbers of the SNR peak sequence, respectively, and N the set of selected gain peak indexes, with K, V and $N \in \mathbb{N}^{n_{SNR}}$. For the case under study,

$$K = (21, 2, 10, 8, 28, 27, 19, 9, 18, 16, 27, 17, 8, 26, 25, 31)^{\mathrm{T}}$$

$$V = (1, 1, 1, 1, 1, 1, 1, 1, 1, 1, 2, 1, 2, 1, 1, 1)^{\mathrm{T}}$$

while N changes from sequence to sequence. A new linear fit in time can therefore be performed on a wider range of nodes, thus refining the fit obtained during the *filtering phase*. We obtain:

$$\min_{\overline{\boldsymbol{u}}, \dot{\boldsymbol{u}}} \sum_{k=1}^{n_{SNR}} \left[\tilde{\boldsymbol{u}}_{N(k)}^{K(k)} - \boldsymbol{u}\left(t^{K(k),V(k)}\right) \right]^{\mathrm{T}} \left[\tilde{\boldsymbol{u}}_{N(k)}^{K(k)} - \boldsymbol{u}\left(t^{K(k),V(k)}\right) \right] \tag{10}$$

At the end of the *linking process*, each candidate sequence is associated with a new estimate for the object track:

$$\widehat{\boldsymbol{u}}(t) = (\Delta\widehat{\gamma}_1(t), \Delta\widehat{\gamma}_2(t))^{\mathrm{T}} = \widehat{\overline{\boldsymbol{u}}}_1 + (t - t_0)\widehat{\dot{\boldsymbol{u}}}_1 \tag{11}$$

23

where the subscript "l" indicates that the estimate is obtained during the *linking process*, while $t \in T_{\text{ill}}$. The result of the *linking process* is shown in Fig. 10b: blue dots are additional gain peaks identified in the *linking process*, and the new estimated track is plotted in blue.

The refined track is then used as a first guess for the second part of the *refinement phase*, here defined *matching process*. The *matching process* can be started if slant range measurements are available. The idea behind the *matching process* is to use the track estimated with Eq. 11 and the available slant range measurements to simulate the SNR profiles of all the illuminated beams. The simulated profiles are then compared with the measured ones, and a nonlinear least-squares process is run to tune the coefficients of the object track to maximize the matching. Unlike the previous phases, here either a linear or a quadratic trend in time is assumed for $\boldsymbol{u}(t)$. By defining with H the set of the identification numbers of all the illuminated beams, $H \in \mathbb{N}^{n_{\text{ill}}}$, $\boldsymbol{SNR}_{\text{obs}}^{H(h)}$ the generic SNR profile measured by beam $H(h)$, and $\boldsymbol{SNR}^{H(h)}$ the simulated SNR profile, one obtains

$$R_1 = \min_{\bar{\boldsymbol{u}}, \dot{\boldsymbol{u}}, RCS} \sum_{h=1}^{n_{\text{ill}}} \left[\boldsymbol{SNR}_{\text{obs}}^{H(h)} - \boldsymbol{SNR}^{H(h)} \right]^{\text{T}} \left[\boldsymbol{SNR}_{\text{obs}}^{H(h)} - \boldsymbol{SNR}^{H(h)} \right] \quad (12)$$

assuming a linear trend for $\boldsymbol{u}(t)$, and

$$R_2 = \min_{\bar{\boldsymbol{u}}, \dot{\boldsymbol{u}}, \ddot{\boldsymbol{u}}, RCS} \sum_{h=1}^{n_{\text{ill}}} \left[\boldsymbol{SNR}_{\text{obs}}^{H(h)} - \boldsymbol{SNR}^{H(h)} \right]^{\text{T}} \left[\boldsymbol{SNR}_{\text{obs}}^{H(h)} - \boldsymbol{SNR}^{H(h)} \right]$$

$$(13)$$

assuming an angular path of the object as

$$\boldsymbol{u}(t) = (\Delta\gamma_1(t), \Delta\gamma_2(t))^{\text{T}} = \bar{\boldsymbol{u}} + (t - t_0)\dot{\boldsymbol{u}} + (t - t_0)^2 \ddot{\boldsymbol{u}} \quad (14)$$

In both least-squares expressions, $\boldsymbol{SNR}^{H(h)} = f(\boldsymbol{u}(t), RCS)$ is a nonlinear function of $\boldsymbol{u}(t)$. During the process, a mean value of the RCS of the objects, which is unknown, is also estimated by including it as an additional fitting parameter. All selected candidate sequences go through the *matching process*, and each sequence is associated with a value of residual $R = \min\{R_1, R_2\}$. This

24

value is used as performance index to identify the best candidate sequence for the object track. At the end of the *matching process*, the candidate with the lowest value of R, R_{best}, is selected as best candidate sequence, and a final estimate for the object track is obtained

$$\widehat{\boldsymbol{u}}(t) = (\Delta\widehat{\gamma}_1(t), \Delta\widehat{\gamma}_2(t))^{\text{T}} = \widehat{\boldsymbol{u}}_{\text{m}} + (t - t_0)\widehat{\boldsymbol{u}}_{\text{m}} + (t - t_0)^2\widehat{\boldsymbol{u}}_{\text{m}} \qquad (15)$$

where the subscript "m" indicates that the estimate is obtained during the *matching process*, while $t \in T_{\text{ill}}$ and $\widehat{\boldsymbol{u}}_{\text{m}} = 0$ if $R_{\text{best}} = R_1$. Figure 10c shows, in magenta, the estimated track at the end of the *refinement phase* for the best candidate sequence: real and estimated tracks coincide up to the plot accuracy.

350 *3.1.3. Critical cases*

The process of track estimation may run into critical cases where it tends to provide inaccurate results. The occurrence of these critical cases strongly depends on the quality of the SNR profile, and may be triggered by strong fluctuations of the detected signal. We offer here a general overview of the 355 possible criticalities, whereas the sensitivity of the algorithm to the SNR profile is studied in detail in Section 4.2.1.

The first critical case concerns passages that involve a symmetry problem. This situation occurs every time only a single column or row of gain peaks is illuminated during the passage of the object. An example is shown in Fig. 11a. 360 In such a situation, the same measured SNR profile is compatible with two passages that are symmetric with respect to the line connecting the gain peaks, but only one of them is the real solution. The first guess of the *matching process* coincides with the symmetry axis, and the resulting track at the end of the nonlinear least-squares process can be either the correct one or its symmetric 365 counterpart: both have the same (low) residual. This situation cannot be solved, but can be detected a priori.

A second critical case is the lack of convergence during the *matching process*. The convergence of the nonlinear least-squares, indeed, strongly depends on the accuracy of the selected first guess for the objects track (i.e. the linear fit
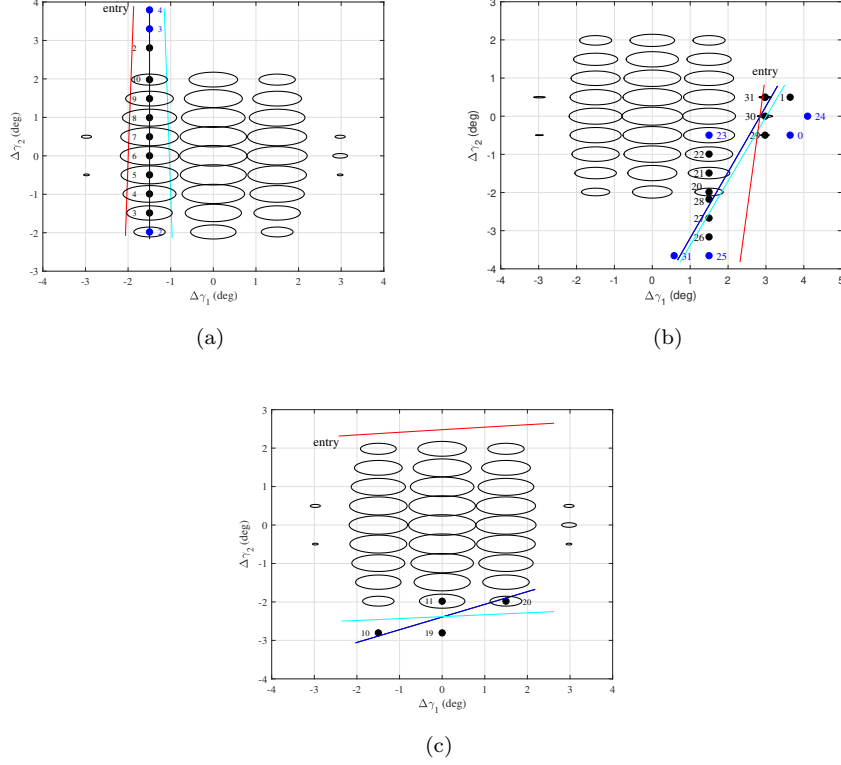
25

Figure 11: Critical cases for the track reconstruction algorithm: (a), symmetry condition (object NORAD ID 1520, passage epoch 15 DEC 2018 02:06:31.775 UTC, El_{RX} 60 deg, North pointing, El_{TX} 40.45 deg, Az_{TX} 7.69 deg), (b), convergence failure (object NORAD ID 28909, passage epoch 15 DEC 2018 22:35:57.821 UTC, El_{RX} 80 deg, South pointing, El_{TX} 72.18 deg, Az_{TX} 28.28 deg), (c), convergence to wrong solution (object NORAD ID 16909, passage epoch 17 DEC 2018 19:16:32.321 UTC, El_{RX} 60 deg, North pointing, El_{TX} 40.45 deg, Az_{TX} 7.69 deg). The red line represents the real passage, the blue line the first guess refined after the *linking process*, the cyan line the result of the *matching process* (1σ *SR* noise level of 10 m, 1σ *SNR* fluctuation level of 0.2 dB, n_{sel} equal to 13).

obtained after the *linking process*), and it may happen that none of the candidate sequences reaches convergence. An example of convergence failure is reported in Fig. 11b. To improve convergence, multiple first guesses are tested. These guesses are obtained by introducing two variations, one in the linear fit process and one in the ranking procedure for the *linking process*. The first variation

consists in performing a weighted linear fit

$$\min_{\bar{\boldsymbol{u}},\dot{\boldsymbol{u}}} \sum_{i=1}^{n_{\text{filt}}} w^i \left[\tilde{\boldsymbol{u}}_{J(i)}^{I(i)} - \boldsymbol{u}\left(t^{I(i)} \right) \right]^{\mathrm{T}} \left[\tilde{\boldsymbol{u}}_{J(i)}^{I(i)} - \boldsymbol{u}\left(t^{I(i)} \right) \right] \tag{16}$$

where $w^i = s^{I(i)}/\max(\boldsymbol{s})$, during the *filtering phase*, and

$$\min_{\bar{\boldsymbol{u}},\dot{\boldsymbol{u}}} \sum_{k=1}^{n_{SNR}} w^k \left[\tilde{\boldsymbol{u}}_{N(k)}^{K(k)} - \boldsymbol{u}\left(t^{K(k),V(k)} \right) \right]^{\mathrm{T}} \left[\tilde{\boldsymbol{u}}_{N(k)}^{K(k)} - \boldsymbol{u}\left(t^{K(k),V(k)} \right) \right] \tag{17}$$

where $w^k = S^{K(k),V(k)}/\max(\boldsymbol{S})$, during the *linking process*.

The second variation is introduced in the ranking procedure of the *linking process* (step 3) and consists in weighting the distance $L_n^{k,v}$ by the gain peak of the considered gain lobe g_n^k.

$$L'^{k,v}_n = L_n^{k,v}/g_n^k \tag{18}$$

These two modifications allow us to slightly change the slope of the first guess for the object track, and significantly reduce the number of convergence failures.

370 The possible convergence to wrong solutions is the last critical condition. Two candidate sequences may turn out to have low residuals, which is typically due to the fact that, during the *matching process*, also the mean RCS is estimated. Therefore, the nonlinear least-squares may in principle change the RCS and obtain low residuals even if the sequence of gain peaks is not the correct

375 one. An example is shown in Fig. 11c.

Unlike symmetric passages, convergence failures and wrong convergences represent the subtlest cases, as they cannot be easily discerned. This is particularly true when the level of SNR fluctuations is high, as the value of the residual at the end of the *refinement phase* cannot be used as a criterion to dis-

380 cern among good and wrong solutions. An analysis of the occurrence of these cases is provided in Section 4.

3.2. Orbital state estimation

The algorithm described in Section 3.1 provides, for each illumination instant, the two estimated angular displacements $\Delta\widehat{\gamma}_1$ and $\Delta\widehat{\gamma}_2$ of the transiting

27

object with respect to the RX pointing direction. These angular profiles, along with the already available slant range and Doppler shift measurements, are then used to estimate the state of the object at the epoch of the first measurement recorded during the passage. A nonlinear least-squares Levenberg-Marquardt batch algorithm is used [19, 20]. A first guess for the orbital state is required, and it is obtained by exploiting the estimated object track. The estimates of the angular deviations in time and the availability of slant range measurements provide an estimate of the Earth Centred Inertial (ECI) position vectors $r_{\mathrm{sat},i}^{\mathrm{ECI}}$ of the object for each illumination instant. By considering two different time instants (for example, the ones of the first and the last recorded measurements), the solution of a simple Lambert's problem provides an estimate for the velocity of the object at the two time epochs, and so a first guess for the state of the object at the epoch of the first recorded measurement $\bar{x}_0$ can be obtained. This first guess is then refined with the nonlinear least-squares process. By defining with $y_{\mathrm{obs}}(t)$ the vector of observations, with

$$y_{\mathrm{obs}}(t) = (DS(t), SR(t), \Delta\widehat{\gamma}_1(t), \Delta\widehat{\gamma}_2(t))^{\mathrm{T}} \tag{19}$$

with $t \in T_{\mathrm{ill}}$, one obtains

$$\min_{x_0} \sum_{t \in T_{\mathrm{ill}}} [y_{\mathrm{obs}}(t) - y(t)]^{\mathrm{T}} [y_{\mathrm{obs}}(t) - y(t)] \tag{20}$$

with $y(t) = g(x(t))$ the nonlinear function mapping the predicted state vector $x(t)$ into the observation space. The mapping from x_0 to $x(t)$ is obtained by integrating the orbital dynamics. Given the very short arcs involved, a simple Keplerian dynamics provides a sufficiently accurate result. The solution of the problem provides an estimate for the state of the transiting object at the epoch of the first recorded measurement $\widehat{x}_0$ and the associated covariance $\widehat{C}_{\widehat{x}_0,\widehat{x}_0}$.

4. Numerical simulations

The orbit determination algorithm described in Section 3 is here applied to assess the performance of BIRALES sensor for IOD in survey mode by means
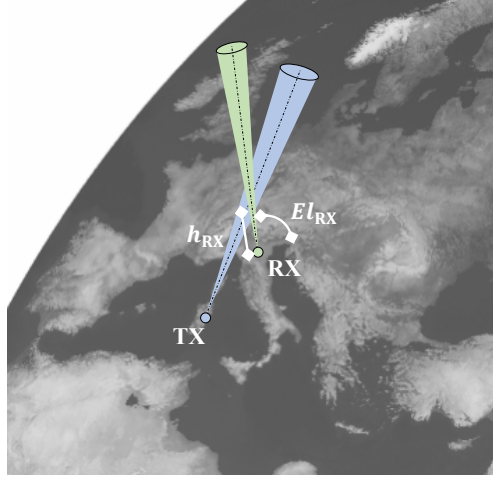
28

Figure 12: BIRALES TX and RX cones intersection as identified by the RX elevation (El_{RX}) and the altitude of the intersection of the two lines of sight (h_{RX}).

of numerical simulations. The first part of the analysis is dedicated to the description of the survey strategy, and the assessment of BIRALES observability performance. The second part investigates the accuracy of the IOD results and the main parameters affecting it.

4.1. Pointing strategy

As mentioned in Section 2, BIRALES RX can be mechanically steered only in elevation, while keeping the azimuth to point either North or South. Therefore, the sensor can mainly detect passages of objects crossing the meridian of the RX. On the other hand, the TX can be moved both in azimuth and elevation, with a minimum elevation of 30 deg. Given the constraints of the sensor and its bistatic configuration, the portion of the sky that can be observed depends on two parameters only: the elevation of the RX, and the altitude of the intersection between the line of sight of the RX and the line of sight of the TX. A sketch of the configuration parameters is shown in Fig. 12. The combination of the two parameters determines the location and the size of the portion of the sky that is covered by the sensor, i.e. the intersection between the FoVs of RX and TX.

29

Table 1: BIRALES sensor characteristics (sensitivity: 25 cm D @ 1000 km range).

	Longitude	Latitude	Altitude
TX	09° 26' 23" E	39° 36' 18" N	684.73 m
RX	11° 38' 45" E	44° 31' 27" N	028.00 m

Though the two FoVs are quite similar is size, due to the bistatic configuration of the sensor, the intersection volume is a sub-fraction of the two full cones. The portion of the sky covered by the sensor increases for higher intersection altitudes. Unfortunately, as the intersection moves higher, the average slant range of observable objects increases as well, which brings about a lower signal measured by the RX. The coverage of the sky is affected also by the elevation. Assuming not to alter the altitude of the intersection point, the intersection volume progressively decreases while passing from North to South pointing.

Given the non uniform distribution of objects around the Earth, the number of observable objects is not directly related to the size of the survey volume covered by the sensor. Thus, the identification of the best pointing strategy is not immediate. In this section, a detailed analysis of the observation capabilities of the sensor is offered. The analysis considers an observation window of one week, from December 15 to December 21, 2018. The dependency on the RX elevation is investigated. For each elevation, the intersection volume maximizing the number of observable objects is selected (see Table 2 for RX and TX pointing directions). A sensitivity of 25 cm diameter (D) @ 1000 km range is assumed for BIRALES (see Table 1). All simulations are carried out considering the satellites and space debris included in the LEO NORAD catalogue as target population and by restricting the analysis to the objects with a known mean RCS value. The resulting overall number of objects is 2727. For each object, the reference Two-Line Elements (TLE) at the beginning of the observation window is downloaded from SPACE-TRACK website [21], and the observation
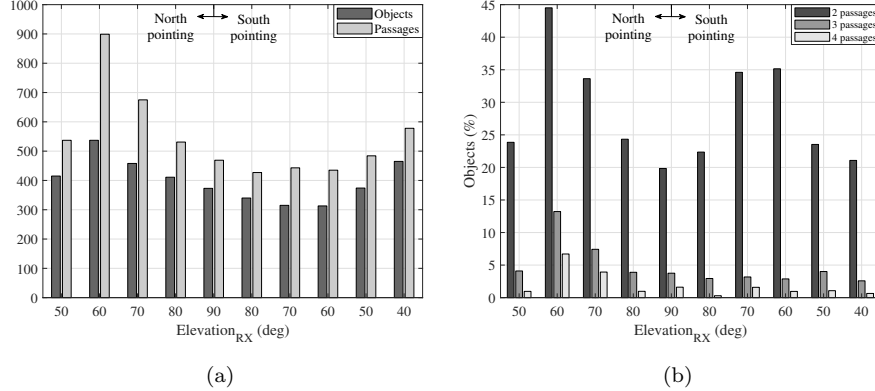
30

Figure 13: BIRALES observation capabilities: (a), number of objects and passages as a function of the RX elevation, (b), percentage of observed objects with at least 2, 3, and 4 passages as a function of the configuration.

capabilities of the sensor are assessed with a dedicated software that propagates the reference TLE and identifies all possible passages of the object in the sensor FoV. The goal of the analysis is to compute the percentage of the catalogue covered by BIRALES sensor in one week of survey operations.

⁴³⁵ Figure 13 shows the results of the analysis considering 10 different elevations of the RX, from 50 deg North (50N) to 40 deg South (40S), with a discretization of 10 deg. Figure 13a shows the number of observed objects and passages as a function of the selected configuration. As can be seen, the selected configurations allow the sensor to observe, on average, from 300 to 500 objects, with the

⁴⁴⁰ upper limit representing about one fifth of the considered catalogue. As a general trend, North pointing configurations guarantee a larger number of observed objects than South pointing configurations. This results is quite expected, as previously mentioned, given the larger intersection volume of the two cones. Nevertheless, the trend is not monotonic: it reaches its maximum at 60N, then

⁴⁴⁵ it progressively decreases till 60S, an then it increases again. The trend of the number of observable passages is similar, though the gain offered by the best configuration with respect to the others is more evident. Furthermore, if one

31

compares the number of observable objects and passages, it is evident that, regardless of the configuration, the number of objects with multiple passages is
450   quite low.

This second aspect is described in more detail in Figure 13b. The plot shows the percentage of objects with at least two, three, and four observed passages with respect to the number of observed objects, as a function of the pointing angles. The plot is quite helpful in defining the observation capabilities of the
455   sensor. As can be seen, while all configurations allow the sensor to re-observe at least one objects out of five, the percentages of re-observed objects drastically decrease as the number of considered passages increases. For example, let us consider the best configuration identified in the previous analysis: out of 537 observed objects, around 44% can be observed at least twice, 13% three times,
460   whereas only 7% of the observed objects has a number of observed passages larger or equal to four. This trend can be easily understood if one refers to the intersection volume of the sensor, and the considered observation window. The number of observed passages per object directly influences the time window between one passage and the next one, which in turn has a strong impact on
465   the evolution of the IOD error in time.

4.2. IOD results

The analysis presented in Section 4.1 focused on the observation capabilities of BIRALES while performing survey operations. This section is dedicated to the analysis of the accuracy of the results obtained when IOD is performed with
470   the sensor. For all the considered pointing configurations and for each passage of any object, no a priori knowledge on the state of the transiting object is assumed to be available. The method described in Section 3 is then applied to perform IOD. A dedicated software for generating simulated measurements was developed and used here. Starting from the available TLE of the object,
475   the software propagates the trajectory with the SGP4 analytical model. At all time instants the object is inside the sensor FoV, for each beam i of the RX, the instantaneous SNR^i value is computed with Eq. 1. If the SNR is larger than

32

the imposed threshold, the values of time instant, SNR and Doppler shift are recorded. For the generation of slant measurements, an upgrade of the sensor is considered, and a single beam covering the whole multibeam FoV is assumed. The result at the end of the passage is a simulated TDM file, containing, for all the illuminated beams, all the illumination instants and the corresponding simulated SNR and Doppler shift, along with slant range measurements. This file represents the starting pointing for all the simulations.

Some measurement error is added to the simulated profiles. A discretization of 9.5 Hz is assumed for Doppler shift measurements, which corresponds to the resolution of the receiving channel. For slant range measurements, the error noise is assumed to be Gaussian with a standard deviation of 10 m [16]. In addition, the ionospheric delay is considered and modelled as an extra uncertainty on the slant range value. More specifically, for each passage, an estimate of the ionospheric delay is obtained by relying on the IRI 2016 model [22]. Starting from the estimated ionospheric delay, an extra error on the slant range is added as Gaussian noise with standard deviation equal to 20% of the estimated ionospheric delay [23]. Error realizations strongly depend on the length of the path followed by the signal in the ionosphere. For the cases under study, ionospheric delays typically are in the order of tens of meters. Finally, the SNR profile is modelled assuming fluctuations of 0.2 dB. The values of the Doppler shift and slant range noise levels are taken from the design requirements of the sensor. The level of SNR fluctuations, instead, is selected in order to simulate profiles with low noise levels and small variations of the RCS of the object during its passage in the FoV of the sensor. Overall, the three noise levels are selected to identify the upper bound of the performance of the sensor. A sensitivity analysis to these quantities is offered later in Section 4.2.1.

Table 2 shows the performance of the track reconstruction method for all the analysed pointing configurations, in terms of symmetric passages (SP) percentage of convergence failures (CF), convergences to wrong solutions (CW). In addition, the median of the root mean square error in $\Delta\gamma_1$ and $\Delta\gamma_2$ ($RMSE_{\Delta\gamma_1}^{50\%}$ and $RMSE_{\Delta\gamma_2}^{50\%}$) is presented as a measure of the angular accuracy of the ob-

33

Table 2: Track reconstruction performance for all considered pointing configurations in terms of symmetric passages (SP), convergence failures (CF), convergences to wrong solutions (CW) and median of the $RMSE$ of $\Delta\gamma_1$ and $\Delta\gamma_2$ ($RMSE_{\Delta\gamma_1}^{50\%}$ and $RMSE_{\Delta\gamma_2}^{50\%}$) ($1\sigma$ SR noise level of 10 m, 1σ SNR fluctuation level of 0.2 dB, n_{sel} equal to 13).

El_{RX} (deg)	Az_{TX} (deg)	El_{TX} (deg)	Passes	SP (%)	CF (%)	CW (%)	$RMSE_{\Delta\gamma_1}^{50\%}$ (deg)	$RMSE_{\Delta\gamma_2}^{50\%}$ (deg)
50N	7.70	29.46	537	4.7	2.2	1.1	4.5e-3	1.4e-3
60N	7.69	40.45	899	2.1	1.1	1.3	3.5e-3	1.0e-3
70N	9.40	48.97	675	1.6	0.1	0.1	4.1e-3	1.0e-3
80N	12.62	56.06	531	1.5	0.4	0.0	4.2e-3	1.2e-2
90	17.78	61.97	469	1.7	0.2	0.0	4.4e-3	1.4e-3
80S	28.28	72.18	427	0.5	0.2	0.5	4.1e-3	1.2e-3
70S	55.35	78.95	443	1.1	0.2	0.0	4.0e-3	1.1e-3
60S	125.80	78.97	435	0.9	0.0	0.2	3.5e-3	1.0e-3
50S	153.27	69.36	484	2.3	0.0	0.2	3.1e-3	9.0e-4
40S	161.80	58.10	578	6.6	0.7	1.0	3.0e-3	1.0e-3

tained track. Symmetric passages are conditions that cannot be controlled, and do not affect all configurations in the same measure. As a general trend, pointing configurations with lower RX elevation show a larger number of symmetric passages. Convergence failures mainly depend on the first guess selected for the track reconstruction method. As can be seen, the multiple first guess approach described in Section 3 allows us to maintain the number of failures below 3%. Also in this case, configurations with higher elevations show the best performance. The most critical condition is represented by the case of convergences to wrong solutions. As can be seen, these cases are quite rare, and mostly occur at low elevations. If the angular accuracy of the obtained track is analysed, we can see that the results show low dependency on the configuration. As a general trend, a better accuracy in $\Delta\gamma_2$ is obtained.
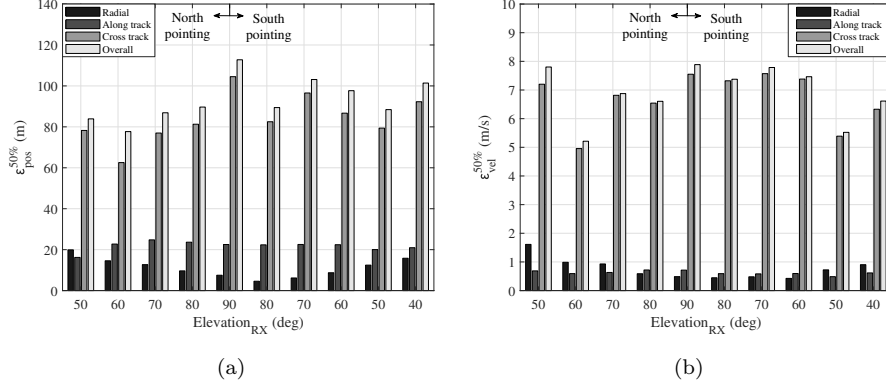
34

Figure 14: BIRALES IOD results accuracy: (a), median of the error in position $\varepsilon_{\text{pos}}^{50\%}$ and (b), median of the error in velocity $\varepsilon_{\text{vel}}^{50\%}$ as a function of the configuration (DS discretization of 9.5 Hz, 1σ SR noise level of 10 m, 1σ SNR fluctuation level of 0.2 dB, n_{sel} equal to 13).

Figure 14 shows the IOD results for BIRALES sensor as a function of the pointing angles in terms of median of the error in position $\varepsilon_{\text{pos}}^{50\%}$ (Fig. 14a) and velocity $\varepsilon_{\text{vel}}^{50\%}$ (Fig. 14b). Errors are expressed both as Euclidean norm of the error vector and RSW (radial, along-track, cross track) components. For the
525 analysis, symmetric passages, i.e. passages labelled as possibly anomalous, are not considered. The analysis of the magnitude of the errors shows an interesting result: the pointing configuration featuring the best performance in terms of observability is also the one granting the best accuracy. Overall, the average error in position is about 90 m, whereas the error in velocity is in the order
530 of some meters per second. The largest errors are obtained in the cross-track direction.

Table 3 summarizes the results of BIRALES sensor in terms of catalogue coverage, percentage of re-observed objects, and IOD results accuracy. All pointing configurations guarantee a good coverage of the catalogue and accurate IOD re-
535 sults. Nevertheless, the constraint on meridian pointing and the small sensor FoV limit the number of objects observed multiple times. This aspect has a negative impact on the accuracy of the evolution of the obtained IOD estimates

Table 3: BIRALES observability and IOD accuracy performance. Re-observed objects are objects for which at least two passages are observed (DS discretization of 9.5 Hz, 1σ SR noise level of 10 m, 1σ SNR fluctuation level of 0.2 dB, n_{sel} equal to 13).

El_{RX} (deg)	Catalogue coverage (%)	Catalogued re-observed objects (%)	$\varepsilon_{\text{pos}}^{50\%}$ (m)	$\varepsilon_{\text{vel}}^{50\%}$ (m/s)
50N	15.22	3.63	83.90	7.80
60N	19.69	8.76	77.68	5.21
70N	16.80	5.65	86.87	6.87
80N	15.07	3.67	89.67	6.61
90	13.69	2.71	112.76	7.89
80S	12.47	2.79	89.42	7.38
70S	11.55	4.00	103.12	7.79
60S	11.48	4.03	97.67	7.46
50S	13.71	3.23	88.42	5.52
40S	17.05	3.59	101.39	6.61

in time, since larger time windows between different passages of the same object lead to larger propagated errors, with possible drawbacks on tracks correlation and catalogue maintenance. Therefore, the analysis suggests that the sensor could play a significant role if integrated in a network of collaborating sensors.

4.2.1. Sensitivity analysis

The accuracy of the IOD result is linked to the accuracy of the estimated angular path and of the Doppler shift and slant range measurements. This section investigates the sensitivity of the algorithm to the accuracy of these parameters. First, the parameters affecting the angular track are investigated. In the second part, the impact of the measurements accuracy on the IOD results is studied.

The results shown in Table 3 are obtained assuming a 1σ SNR fluctuation

level of 0.2 dB. This value corresponds to a low noise level and small variations of the RCS during the transit of the object in the RX FoV. Though strong, this second assumption is not totally unrealistic, given the small FoV of the sensor, which in many cases leads to passages of just few seconds. Certainly, it provides an upper bound of the performance of the algorithm. It is therefore interesting to study what happens for larger variations of the RCS during the passage of the object. A dedicated sensitivity analysis is here presented. The RCS variation is modelled as additional SNR noise. Four different 1σ SNR noise levels are considered: 0.2 dB (i.e. negligible variations of the RCS), 0.5 dB, 1 dB and 2 dB. The analysis considers only one RX configuration, the 60N configuration, i.e. the one granting the largest number of passages and the best IOD performance.

The first consequence of larger fluctuations of the RCS during the passage of the object in the RX FoV is a drop in accuracy of the estimated track. The presented algorithm can estimate only a mean value of the object RCS (see Section 3.1.2), and a strong fluctuation may lead to larger residuals obtained at the end of the *refinement phase*. Figure 15a shows an example of angular accuracy dependency as a function of the level of SNR fluctuations. In some cases, the fluctuations may be so large that, even if the algorithm identifies the right illumination sequence, it cannot converge. The convergence of the algorithm, indeed, strongly depends on the accuracy of the provided first guess. The multiple first guess solution described in Section 3.1.3 fails in case of strong fluctuations of the RCS during the passage of the object. RCS fluctuations, therefore, exacerbate the already existing problem of convergence failures. Figure 15b shows an example of this problem: the algorithm converges to the right solution up to a noise level of 1 dB, whereas it cannot converge with a noise level of 2 dB. In the worst case scenario, a strong variation of the RCS may cause the algorithm to provide a wrong illumination sequence and, thus, a completely wrong track estimate.

Table 4 summarizes the results of the sensitivity analysis. The results are expressed in terms of number of symmetric passages, convergence failures, con-
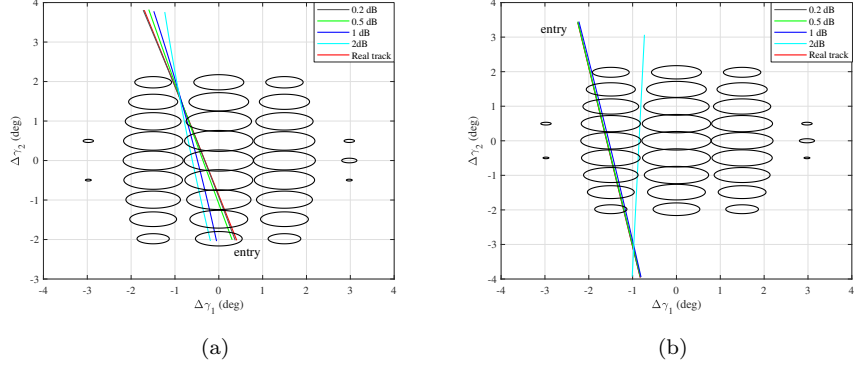
37

Figure 15: Track reconstruction algorithm dependency on SNR fluctuation level: (a), angular accuracy (object NORAD ID 3891, passage epoch 19 DEC 2018 23:24:00.551 UTC), (b), convergence success (object NORAD ID 40920, passage epoch 18 DEC 2018 16:58:29.443 UTC), (1σ SR noise level of 10 m, n_{sel} equal to 13, El_{RX} 60 deg, North pointing, El_{TX} 40.45 deg, Az_{TX} 7.69 deg).

Table 4: BIRALES IOD accuracy performance as a function of the SNR noise level in terms of symmetric passages (SP), convergence failures (CF), convergences to wrong solutions (CW), median of the $RMSE$ of $\Delta\gamma_1$ and $\Delta\gamma_2$ ($RMSE_{\Delta\gamma_1}^{50\%}$ and $RMSE_{\Delta\gamma_2}^{50\%}$), median of the error in position and velocity $\varepsilon_{\text{pos}}^{50\%}$ and $\varepsilon_{\text{vel}}^{50\%}$ (El_{RX} 60 deg, North pointing, El_{TX} 40.45 deg, Az_{TX} 7.69 deg, DS discretization of 9.5 Hz, 1σ SR noise level of 10 m, n_{sel} equal to 13).

1σ Noise (dB)	SP (%)	CF (%)	CW (%)	$RMSE_{\Delta\gamma_1}^{50\%}$ (deg)	$RMSE_{\Delta\gamma_2}^{50\%}$ (deg)	$\varepsilon_{\text{pos}}^{50\%}$ (m)	$\varepsilon_{\text{vel}}^{50\%}$ (m/s)
0.2	2.1	1.1	1.3	3.5e-3	1.0e-3	77.7	5.2
0.5	1.6	2.2	0.7	1.0e-2	2.7e-3	235.6	17.3
1	1.2	4.9	0.8	2.4e-2	5.7e-3	612.6	42.6
2	1.3	10.7	1.3	6.7e-2	1.2e-2	1613.7	124.2

vergences to wrong solutions, median of the $RMSE$ of $\Delta\gamma_1$ and $\Delta\gamma_2$ and median of the error in position and velocity. As expected, as the level of SNR fluctuations increases, the performance of the algorithm worsens. This is clear if we
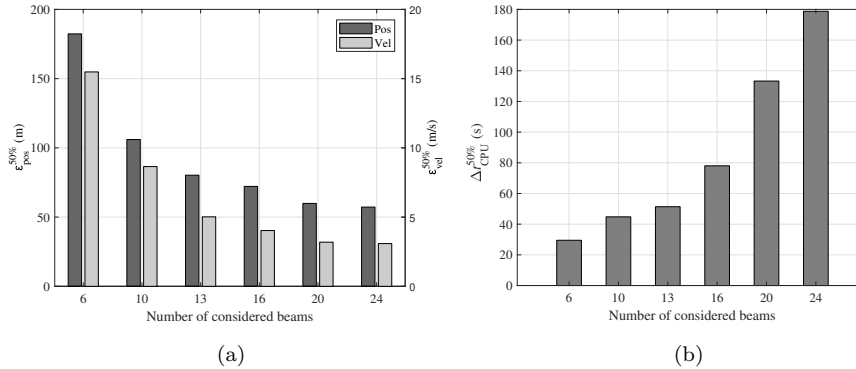
(a)   (b)

Figure 16: Dependency of BIRALES IOD performance on the number of considered beams: (a), accuracy, (b), computational time $\Delta t_{\text{CPU}}^{50\%}$ (El_{RX} 60 deg, North pointing, El_{TX} 40.45 deg, Az_{TX} 7.69 deg, DS discretization of 9.5 Hz, 1σ SR noise level of 10 m, 1σ SNR fluctuation level of 0.2 dB).

look at both the larger number of convergence failures and, overall, the larger

585 $RMSE$ of the two angular estimates. As a consequence, the accuracy of the IOD estimates decreases as well, with an error in position passing from about 80 m to 1.6 km. It is worth noting, however, that, while a 0.2 dB level represents a quite optimistic assumption, 2 dB offers a quite pessimistic scenario, in which each SNR profile shows 1σ fluctuations of $\pm 60\%$ with respect to the ideal case

590 of constant RCS and negligible noise signal in a time frame of 0.1 s. Therefore, the first and last line of Table 4 can be deemed to provide the upper and lower bound performance of the algorithm for realistic scenarios.

Another critical aspect for the estimation of the angular path is the number of considered beams. As described in Section 3, one of the available parameters

595 for track reconstruction is the level of the preliminary threshold adopted for the SNR cut. Figure 16a shows the dependency of the IOD accuracy on the number of considered beams n_{sel} for the pointing configuration granting the best performance (60N). As can be seen, the accuracy improves as the number of considered beams increases. As a drawback, the required computational time

600 increases accordingly (see Fig. 16b). When performing statistical simulations on

39

Table 5: BIRALES IOD accuracy performance as a function of the DS resolution in terms of symmetric passages (SP), convergence failures (CF), convergences to wrong solutions (CW), median of the $RMSE$ of $\Delta\gamma_1$ and $\Delta\gamma_2$ ($RMSE^{50\%}_{\Delta\gamma_1}$ and $RMSE^{50\%}_{\Delta\gamma_2}$), median of the error in position and velocity $\varepsilon^{50\%}_{\text{pos}}$ and $\varepsilon^{50\%}_{\text{vel}}$ (El_{RX} 60 deg, North pointing, El_{TX} 40.45 deg, Az_{TX} 7.69 deg, 1σ SR noise level of 10 m, 1σ SNR fluctuation level of 1 dB, n_{sel} equal to 13).

DS resolution (Hz)	SP (%)	CF (%)	CW (%)	$RMSE^{50\%}_{\Delta\gamma_1}$ (deg)	$RMSE^{50\%}_{\Delta\gamma_2}$ (deg)	$\varepsilon^{50\%}_{\text{pos}}$ (m)	$\varepsilon^{50\%}_{\text{vel}}$ (m/s)
9.5	1.2	4.9	0.8	2.4e-2	5.7e-3	612.6	42.6
20	1.2	4.9	0.8	2.4e-2	5.7e-3	602.3	48.8
30	1.2	4.9	0.8	2.4e-2	5.7e-3	581.4	49.4

Table 6: BIRALES IOD accuracy performance as a function of the SR uncertainty in terms of symmetric passages (SP), convergence failures (CF), convergences to wrong solutions (CW), median of the $RMSE$ of $\Delta\gamma_1$ and $\Delta\gamma_2$ ($RMSE^{50\%}_{\Delta\gamma_1}$ and $RMSE^{50\%}_{\Delta\gamma_2}$), median of the error in position and velocity $\varepsilon^{50\%}_{\text{pos}}$ and $\varepsilon^{50\%}_{\text{vel}}$ (El_{RX} 60 deg, North pointing, El_{TX} 40.45 deg, Az_{TX} 7.69 deg, DS discretization of 9.5 Hz, 1σ SNR fluctuation level of 1 dB, n_{sel} equal to 13).

1σ SR (m)	SP (%)	CF (%)	CW (%)	$RMSE^{50\%}_{\Delta\gamma_1}$ (deg)	$RMSE^{50\%}_{\Delta\gamma_2}$ (deg)	$\varepsilon^{50\%}_{\text{pos}}$ (m)	$\varepsilon^{50\%}_{\text{vel}}$ (m/s)
10	1.2	4.9	0.8	2.4e-2	5.7e-3	612.6	42.6
30	1.2	4.9	0.8	2.5e-2	5.7e-3	573.5	46.3
60	1.2	4.9	0.8	2.5e-2	5.7e-3	616.1	47.4

a large number of objects, it is reasonable to select a threshold granting a good trade-off between accuracy and computational effort. The analyses reported here were carried out by imposing a number of considered beams equal to 13.

While the level of SNR fluctuations and the number of selected beams directly affect the accuracy of the estimated track and, as a consequence, the IOD results, the effect of inaccurate Doppler shift and slant range measure-

ments is different. Doppler shift inaccuracies affect the IOD result only; no effect on the estimated track is obtained. A larger noise in the slant range measurements, instead, may affect both the track reconstruction and the state estimation phase, as slant range measurements are used in both the *refinement phase* and the nonlinear least squares process described in Section 3.2. Doppler shift and slant range inaccuracy may arise from range and Doppler migration phenomena. Depending on the bistatic acceleration of the transiting target, it may happen that the signal acquired by the multibeam radar system is spread over more frequency channels. At present, the problem is faced by selecting the channel with the highest measured SNR. Typically, this channel is the central one. This phenomenon may of course lead to Doppler shift uncertainties that are larger than the theoretical frequency resolution. In parallel, slant range measurements may be affected by range migration phenomena. Tables 5 and 6 show the performance of the algorithm considering the 60N configuration and increasing values of DS resolution (9.5 Hz, 20 Hz, 30 Hz) and 1σ SR noise level (10 m, 30 m, 60 m), with a value of 1σ SNR fluctuation level of 1 dB and n_{sel} equal to 13. As can be seen, the effect of both quantities is almost negligible both in position and velocity accuracy. That is, when the level of SNR noise is large, the final accuracy of the IOD result is mainly governed by the accuracy of the estimated track.

5. Conclusions

This paper described in detail the architecture and the performance of the Italian bistatic radar sensor BIRALES for space surveillance. The sensor combines a single-beam pulse compression system and a multibeam CW unmodulated radar which enables the reconstruction of the track of the transiting object in the RX FoV and the precise estimation of its orbital parameters with just a single passage. An accurate description of the dedicated track reconstruction algorithm was offered, and all the critical cases were discussed in detail. The space surveillance potential of the sensor was then investigated via numerical

41

simulations. The dependency of the performance on the pointing angles was studied. Finally, the IOD accuracy was assessed. The sensor grants good catalogue coverage and sufficiently accurate IOD results obtained with no a priori knowledge of state and physical properties of the transiting object. However, the current version of the algorithm shows a quite significant sensitivity to possible strong variations of the object radar cross section during its passage in the RX FoV. Furthermore, the peculiar configuration of the sensor limits the number of re-observed objects. Consequently, to fully exploit its potential, the sensor requires an increase of the FoV, which is currently underway, and needs to be integrated into a network of sensors that can guarantee the execution of follow-up observations. The system is currently being tested on the analysis of measurement data obtained during real observation campaigns carried out both in tracking and survey mode. In parallel, catalogue correlation performance using BIRALES sensor data is being studied.

Acknowledgements

42

References

[1] ESA Space Debris Office, ESA's Annual Space Environment Report, techreport, European Space Agency (May 2019).
URL https://www.sdo.esoc.esa.int/environment_report/Space_Environment_Report_latest.pdf

[2] ESA: space debris by the numbers, https://www.esa.int/Our_Activities/Operations/Space_Safety_Security/Space_Debris/Space_debris_by_the_numbers, accessed: 2019-04-16.

[3] D. J. Kessler, Collisional cascading: the limits of population growth in Low Earth Orbit, Advances in Space Research 11 (12) (1991) 63–66. doi:10.1016/0273-1177(91)90543-S.

[4] K. Merz, B. Bastida Virgili, V. Braun, T. Flohrer, Q. Funke, H. Krag, S. Lemmens, Current collision avoidance service by ESA's Space Debris Office, in: Proc. of the 7th European Conference on Space Debris, 2017.

[5] B. Bastida Virgili, S. Lemmens, J. Siminski, Q. Funke, T. Flohrer, Combining observations for re-entry purposes, in: Proc. of the 1st NEO and Debris Detection Conference, 2019.

[6] European Union Law, `https://eur-lex.europa.eu/legal-content/GA/TXT/?uri=CELEX:32014D0541`, accessed: 2019-04-16.

[7] ESA: Space Situational Awareness, `http://www.esa.int/Our_Activities/Operations/Space_Situational_Awareness/About_SSA`, accessed: 2019-04-16.

[8] A. Morselli, P. Di Lizia, G. Bianchi, C. Bortolotti, S. Montebugnoli, G. Naldi, F. Perini, G. Pupillo, M. Roma, M. Schiaffino, A. Mattana, E. Salerno, A. Magro, K. Z. Adami, R. Armellin, A. L. Sergiusti, W. Villadei, F. Dolce, M. Reali, J. Paoli, A new high sensitivity radar sensor for space debris detection and accurate orbit determination, in: Metrology for Aerospace (MetroAeroSpace), 2015.

[9] M. Losacco, P. Di Lizia, M. Massari, A. Mattana, F. Perini, M. Schiaffino, C. Bortolotti, M. Roma, G. Naldi, G. Pupillo, G. Bianchi, L. Lama, D. Cutajar, A. Magro, C. Portelli, M. Reali, W. Villadei, The multibeam radar sensor BIRALES: Performance assessment for space surveillance and tracking, in: Proc. of the 69th International Astronautical Congress, 2018.

[10] G. Bianchi, C. Bortolotti, A. Cattani, F. Fiocchi, A. Maccaferri, A. Mattana, M. Morsiani, G. Naldi, F. Perini, A. Porfido, G. Pupillo, M. Roma, S. Rusticelli, M. Schiaffino, E. Urru, P. Di Lizia, M. Losacco, M. Massari, J. Borg, D. Cutajar, A. Magro, M. Reali, W. Villadei, A new approach to LEO space debris survey: the italian multibeam bi-static radar BIRALES, in: Proc. of the 1st IAA Conference on Space Situational Awareness (IC-SSA), 2017.

[11] L. Pucker, Channelization techniques for software defined radio, in: Proc. of the SDR Forum Conference, 2003.

[12] M. Ester, H.-P. Kriegel, J. Sander, X. Xu, A Density-Based Algorithm for Discovering Clusters in Large Spatial Databases with Noise, in: KDD-96 Proc., 1996.

44

[13] The Consultative Committee for Space Data Systems: Tracking Data Messages, `https://public.ccsds.org/Pubs/503x0b1c1.pdf`, accessed: 2019-05-05.

[14] M. I. Skolnik, Radar Handbook, McGraw Hill, 1990.

[15] D. Cutajar, A. Magro, J. Borg, K. Zarb Adami, G. Bianchi, C. Bortolotti, A. Cattani, F. Fiocchi, L. Lama, A. Mattana, M. Morsiani, G. Naldi, F. Perini, G. Pupillo, M. Roma, S. Rusticelli, M. Schiaffino, P. Di Lizia, M. Losacco, M. Massari, M. Reali, W. Villadei, A real-time space debris detection system for BIRALES, Journal of British Interplanetary Society 71 (2018) 102–108.

[16] T. Pisanu, L. Schirru, E. Urru, F. Gaudiomonte, P. Ortu, G. Bianchi, C. Bortolotti, M. Roma, G. Muntoni, G. Montisci, F. Protopapa, A. Podda, A. Sulis, Upgrading the Italian BIRALES System to a Pulse Compression Radar for Space Debris Range Measurements, in: Proc. of the 22nd International Microwave and Radar Conference (MIKON), 2018.

[17] L. Scharf, Statistical signal processing: detection, estimation, and time series analysis, Addison-Wesley Pub. Co., 1991.

[18] W. L. Stutzman, G. A. Thiele, Antenna Theory and Design, 3rd Edition, 2013, Ch. 8, p. 307.

[19] K. Levenberg, A method for the solution of certain non-linear problems in least squares, Quart. Appl. Math. 2 (2) (1944) 164–168. `doi:10.1090/qam/10666`.

[20] D. Marquardt, An algorithm for least-squares estimation of nonlinear parameters, J. Soc. Indust. Appl. Math 11 (2) (1963) 431–441. `doi:10.1137/0111030`.

[21] Space-track, `https://www.space-track.org`, accessed: 2018-12-14.

[22] D. Bilitza, IRI the international standard for the ionosphere, Advances in Radio Science 16 (2018) 1–11. `doi:10.5194/ars-16-1-2018`.

[23] I. V. Krasheninnikov, N. M. Pavlova, Y. S. Sitnov, IRI model in the problem of predicting ionospheric radio-wave propagation under conditions of high solar activity, Geomagnetism and Aeronomy 57 (6) (2017) 719–726. `doi: 10.1134/S0016793217060056`.

750